

# Federated Learning with Partially Labeled Data: A Conditional Distillation Approach

Pochuan Wang<sup>1</sup>, Chen Shen<sup>2</sup>, Masahiro Oda<sup>2</sup>, Chiou-Shann Fuh<sup>1</sup>,  
Kensaku Mori<sup>2,\*</sup>, Weichung Wang<sup>1,\*</sup>, Holger R. Roth<sup>3,\*</sup>  
<sup>1</sup>National Taiwan University, <sup>2</sup>Nagoya University, <sup>3</sup>NVIDIA Corp.

## Abstract

In medical imaging, developing generalized segmentation models that can handle multiple organs and lesions is crucial. However, the scarcity of fully annotated datasets and strict privacy regulations present significant barriers to data sharing. Federated Learning (FL) allows decentralized model training, but existing FL methods often struggle with partial labeling, leading to model divergence and catastrophic forgetting. We propose ConDistFL, a novel FL framework incorporating conditional distillation to address these challenges. ConDistFL enables effective learning from partially labeled datasets, significantly improving segmentation accuracy across distributed and non-uniform datasets. In addition to its superior segmentation performance, ConDistFL maintains computational and communication efficiency, ensuring its scalability for real-world applications. Furthermore, ConDistFL demonstrates remarkable generalizability, significantly outperforming existing FL methods in out-of-federation tests, even adapting to unseen contrast phases (e.g., non-contrast CT images) in our experiments. Extensive evaluations on 3D CT and 2D chest X-ray datasets show that ConDistFL is an efficient, adaptable solution for collaborative medical image segmentation in privacy-constrained settings.

Our code is publicly available in NVIDIA FLARE: <https://nvidia.github.io/NVFlare/research/condist-fl>.

**Keywords:** Federated Learning, Partially labeled data, Knowledge distillation, Multi-organ segmentation

\*

## 1 Introduction

Multiorgan segmentation plays a pivotal role in medical imaging, with applications such as disease diagnosis, treatment planning, and surgical guidance. Accurate segmentation of multiple organs in both 2D and 3D medical images is essential for these tasks, driving extensive research in this field. However, obtaining fully annotated datasets for training segmentation models is challenging due to the high cost and specialized expertise required for medical image annotation, particularly from experienced radiologists. Moreover, privacy concerns

surrounding medical data further complicate the process of combining datasets from multiple institutions, particularly when data sharing is restricted by legal and ethical constraints (Rieke et al., 2020).

Existing datasets, such as Beyond the Cranial Vault (Landman et al., 2015) (BTCV), AMOS22 (Ji et al., 2022), and TotalSegmentor (Wasserthal et al., 2023), offer segmentation labels for multiple organs. However, these datasets are often inconsistent in the organs they label, making it difficult to combine them for training comprehensive multiorgan segmentation models. Additionally, most datasets do not provide detailed annotations for abnormal or lesion areas within organs, with notable exceptions like the Medical Segmentation Decathlon (Antonelli et al., 2021) (MSD) and 2019 Kidney Tumor Segmentation Challenge (Heller

\*Corresponding Authors

et al., 2021) (KiTS19). The ability to segment both healthy tissues and lesions is crucial for broader clinical applicability, yet such annotations are often incomplete.

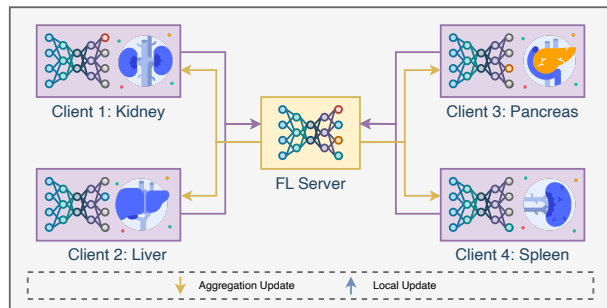


Figure 1: An illustration of the federated learning setup for multi-organ and tumor segmentation using partially labeled datasets. Each client has annotations for only a subset of the targeted organs and malignancies in their local datasets.

Federated learning (FL) has emerged as a promising solution to address both the privacy challenges and the need for collaborative model development without sharing data (Yang et al., 2019). FL enables the training of robust models by leveraging distributed datasets across institutions without requiring direct access to the data itself. Studies have shown FL’s effectiveness in medical image segmentation, particularly for applications in abdominal organ segmentation (Wang et al., 2020; Czeizler et al., 2020), brain tumor analysis (Sheller et al., 2019; Li et al., 2019; Correia de Verdier et al., 2024), and COVID-19 imaging (Dou et al., 2021; Dayan et al., 2021; Xia et al., 2021). However, applying FL to partially labeled datasets (see Fig. 1) introduces additional challenges, particularly with FL model divergence and catastrophic forgetting of unlabeled organs, which degrade overall performance. Furthermore, current approaches often rely on customized segmentation models, leading to increased training complexity and reduced flexibility for adopting newer architectures.

In this paper, we propose ConDistFL, a novel federated learning approach that addresses these challenges by integrating conditional distillation into the FL framework. ConDistFL effectively mitigates model divergence and catastrophic forgetting, enabling

accurate segmentation of both labeled and unlabeled organs. This approach not only enhances segmentation performance across diverse datasets but also maintains computational efficiency, making it a practical solution for real-world medical image segmentation tasks.

This work extends our earlier report (Wang et al., 2023) presented at a scientific workshop. In this journal paper, we have made significant improvements in three key aspects:

- **Enhanced Backbone Integration:** We integrated the advanced MedNeXt segmentation backbone into the ConDistFL framework, resulting in superior segmentation performance and improved generalizability, as demonstrated on a large, unseen test set.
- **Extended 2D Evaluation:** We expanded our evaluation to include 2D segmentation tasks, demonstrating the robustness and versatility of ConDistFL across different imaging modalities and scenarios.
- **Comprehensive Performance Analysis:** We conducted an in-depth analysis of ConDistFL’s performance, providing detailed insights into its effectiveness in preventing model divergence and catastrophic forgetting and highlighting its practical benefits for real-world medical imaging applications.

## 2 Related Works

In this section, we review the key advancements relevant to our study, particularly focusing on segmentation models and federated learning approaches. We begin by discussing segmentation backbones developed for fully annotated datasets, followed by a review of centralized learning strategies for partially labeled datasets. Finally, we examine FL solutions designed for scenarios where annotations are incomplete or limited.

### 2.0.1 Models for Medical Image Segmentation

U-Net-based models (Ronneberger et al., 2015; Milletari et al., 2016; Zhou et al., 2018; Isensee et al., 2021) are widely used in medical image segmentation due to their effectiveness across various tasks. Among

these, nnU-Net (Isensee et al., 2021) stands out with its self-configuring framework, which adapts to dataset characteristics and establishes a robust preprocessing and training pipeline, making it a standard in both competitions and real-world applications.

Recent advances include hybrid models that integrate CNNs and transformers, such as UNetR (Hatamizadeh et al., 2022), which uses a Vision Transformer (ViT) encoder, and SwinUNetR (Hatamizadeh et al., 2021), which employs the SwinTransformer encoder. These models offer improved performance and computational efficiency compared to traditional U-Nets, particularly with larger datasets.

Additionally, MedNeXt (Roy et al., 2023a), a model using ConvNeXt blocks in a U-Net architecture, has shown superior performance over other CNN-based or Transformer-based models on several benchmark datasets (Isensee et al., 2024), demonstrating the continued strength of CNN-based architectures in medical image segmentation.

### 2.0.2 Centralized Learning for Partially Labeled Datasets

Several centralized learning approaches have been developed to address the challenges of using multiple partially labeled datasets for medical image segmentation. These methods often focus on specialized loss functions, task-specific model adaptations, and incremental learning to manage label inconsistencies across datasets.

A common approach involves customizing loss functions to prevent label conflicts during training. For example, marginal loss and exclusive loss (Shi et al., 2021) have effectively ensured consistent learning from partially labeled data using general segmentation models. Similarly, PIPO-FAN (Fang and Yan, 2020) utilizes a customized multi-scale U-shaped architecture with image pyramid inputs and proposes a target adaptive loss to integrate partially labeled datasets.

Another strategy involves model designs like DoDNet (Zhang et al., 2021), and TransDoDNet (Xie et al., 2023), which allow for task-specific queries, enabling the model to dynamically adapt to different target organs. Pseudo-labeling techniques, such as those used in COSST (Liu et al., 2024), introduce a self-training loop to generate and refine labels for unlabeled data,

improving segmentation accuracy over time.

Incremental learning approaches (Liu et al., 2022; Ji et al., 2023) have also been explored, allowing models to continuously integrate new datasets while maintaining performance on previously learned tasks. Additionally, CLIP-driven models, like the CLIP-driven Universal Model (Liu et al., 2023), leverage contrastive language-image pre-training to incorporate text embeddings into the segmentation process. This approach overcomes label limitations through masked back-propagation, offering flexibility in handling partial annotations.

While these centralized methods effectively integrate multiple datasets with inconsistent labels, they often face privacy challenges in medical applications, where direct data sharing is restricted. As a result, they may not fully address the privacy concerns required for real-world medical datasets.

### 2.0.3 Federated Learning for Partially Labeled Datasets

In contrast to centralized learning, federated learning for partially labeled datasets involves distributing data across multiple sites (clients), each with different label definitions. This decentralized setup introduces additional challenges, such as model divergence due to non-i.i.d. data distributions and catastrophic forgetting of unlabeled classes when models are fine-tuned on clients with only partially labeled data.

Our previous work (Shen et al., 2022) tackled these challenges by employing the C2FNAS (Yu et al., 2020) model and using sigmoid activation to avoid label conflicts across clients. While this approach mitigated label inconsistencies, it suffered from significant model divergence during local training, resulting in suboptimal performance of the global model.

Several other customized FL models have been proposed to address the challenges of partially labeled data. MenuNet (Xu et al., 2023) employs multiple encoders, assigning one encoder per organ to handle the non-i.i.d. nature of data across clients. Similar to our earlier approach, it uses sigmoid activation to resolve label conflicts. However, this model faces scalability issues—its training complexity and GPU memory requirements grow with the number of organs. Additionally, MenuNet relies on a client with a fully annotated

Table 1: Summary and comparisons to related works for FL partial labeled segmentation methods for abdominal CT datasets.

Method	Data			Model	
	#Organs	Fully Annotated Dataset	Tumor Segmentation	Input Type	Custom Architecture
C2FNAS+Sigmoid (Shen et al., 2022)	4	Test Only	Yes	3D	Not required
MenuNet (Xu et al., 2023)	4	Train and Test	No	3D	Organ-specific encoder
FedIOD (Wan et al., 2024)	3	Test Only	No	2D	Organ-specific decoder with cross-organ attention module
Kim et al. (Kim et al., 2024)	7	Test Only	Yes	3D	Organ-specific segmentation head
ConDistFL (Ours)	4	Test Only	Yes	3D	Not Required

dataset, limiting its flexibility in real-world scenarios.

FedIOD (Wan et al., 2024) proposes a shared encoder with multiple decoders and utilizes transformers to aggregate cross-client inter-organ dependencies. This design aims to mitigate model divergence while addressing inter-organ relationships. However, like MenuNet, its computational requirements increase with the number of organs, and its evaluations are limited to kidney, liver, and pancreas datasets, restricting its generalizability.

Another promising approach is the knowledge distillation framework proposed by Kim et al. (Kim et al., 2024), which uses a shared model backbone with lightweight segmentation heads for each organ. It combines global and local knowledge distillation to avoid catastrophic forgetting, using cross-entropy loss between the global model and local models (global distillation) as well as pre-trained models from other clients (local distillation). This method can segment both organs and tumors, but it requires a customized model architecture. Additionally, the distillation process forces the local model to fit multiple probability distributions simultaneously, which can lead to conflicts when model outputs disagree.

Table 2.0.3 summarizes the key differences among these approaches, comparing factors such as the use of fully annotated datasets, the ability to segment tumor regions, the input type (2D slices or 3D volumes), and whether a customized model architecture is required. This table provides a concise overview of the distinctions between ConDistFL and the related methods discussed.

A key takeaway from these studies is that using softmax activation, as in FedIOD (Wan et al., 2024), offers a better interpretation of the non-overlapping nature of the anatomy appearance in medical images compared to sigmoid activation, which treats organ segmentation as an independent task. Moreover, only a few approaches – such as our previous work (Shen et al.,

2022) and Kim et al. (Kim et al., 2024) – evaluate tumor segmentation performance, whereas most other methods focus solely on whole organ segmentation.

### 3 Method

This study introduces ConDistFL, an FL framework designed for multi-organ segmentation in medical images. The primary challenge addressed is the partial labeling across different clients, where each client’s dataset contains labels for only a subset of the total organ classes. The proposed method integrates a novel Conditional Distillation (ConDist) loss with traditional supervised learning to enhance the performance and generalizability of segmentation models in a federated setting.

Let  $\mathcal{F}$  represent the segmentation model, which aims to identify  $N$  classes of regions of interest (ROIs) across  $K$  clients, including the background. For an image  $x_k$  in client  $k \in \{1, \dots, K\}$ , only a subset of these  $N$  classes are annotated by radiologists in its corresponding label  $y_k$ , denoted as the foreground classes  $F_k$  for client  $k$ . The set of remaining classes, including the background class 0 and all unlabeled classes for client  $k$ , is denoted as  $B_k$ . The union of all foreground classes across clients must collectively cover all  $N-1$  non-background classes, ensuring that  $|F_1 \cup F_2 \cup \dots \cup F_K| = N-1$ .

#### 3.1 Output Activation and Softmax Function

In multi-organ segmentation, each pixel in an image must be assigned exclusively to one of the  $N$  classes, as human organs do not overlap. To enforce this constraint, we adopt the softmax function  $\sigma$  (Equation 1) as the output activation. This function transforms the output

logits into a probability distribution over the  $N$  classes, ensuring that the model’s output reflects the mutually exclusive nature of organ segmentation.

$$\sigma_i(z) = \frac{e^{z_i}}{\sum_{j=1}^N e^{z_j}} \quad (1)$$

The use of softmax differs from a sigmoid-based activation, where each class would be treated independently. The softmax formulation prevents overlapping segmentations and encourages the model to learn spatial relationships between different organs.

### 3.2 Training Process and Loss Functions

The ConDistFL training process, as illustrated in Figure 2, involves two key components: a supervised learning loss  $\mathcal{L}_{sup}$  (details in Section 3.3) and a ConDist loss  $\mathcal{L}_{ConDist}$  (details in Section 3.4). The supervised loss handles the labeled data available at each client, while the ConDist loss leverages the global model’s predictions to enhance the local model’s performance on unlabeled classes.

### 3.3 Supervised Learning Loss

One key challenge in FL with partially labeled data is that unlabeled classes in  $B_k$  are incorrectly assigned to the background class. This erroneous assignment introduces inconsistencies in target definitions across clients, negatively impacting FL convergence. To mitigate this issue, we adopt the marginal loss (Shi et al., 2021), which adjusts the probability distributions of both the ground truth labels  $y_k$  and the model’s predicted output  $\hat{y}_k$ . Here,  $y_k$  represents the one-hot encoded ground truth, while  $\hat{y}_k = \sigma(\mathcal{F}_k(x_k))$  is the softmax-normalized output of the local model on client  $k$ .

The marginal loss approach preserves the probability distribution of the foreground classes  $F_k$  while accumulating the probability mass for the background and the unlabeled classes in  $B_k$ . This ensures that unlabeled classes are not mistakenly assigned to the background category, effectively resolving the label conflict across clients. We implement this by combining marginal Dice loss with cross-entropy loss, optimizing the model for segmentation performance.

## 3.4 Conditional Distillation Loss

The ConDist loss  $\mathcal{L}_{ConDist}$  aims to minimize the discrepancy between the global model’s predictions and the local model’s predictions for the unlabeled classes. This loss is similar to knowledge distillation, where the softmax function is used with a temperature parameter  $\tau$  to smooth the output probability distributions. Let  $\hat{y}_g^\tau = \sigma(\mathcal{F}_g(x_k)/\tau)$  denote the global model’s smoothed output, and  $\hat{y}_k^\tau = \sigma(\mathcal{F}_k(x_k)/\tau)$  denote the local model’s smoothed output for client  $k$ .

The ConDist loss is composed of the following key techniques:

#### 3.4.1 Foreground Class Grouping

The ConDist loss primarily targets optimizing the background classes  $B_k$ , and therefore, the class-specific probabilities associated with the foreground classes  $F_k$  become secondary in this context. To manage this, we adopt a grouping technique akin to the marginal loss approach, which aggregates the probabilities for the foreground classes. We denote these aggregated probabilities for the global and local models as  $\hat{y}_{g,F_k}^\tau$  and  $\hat{y}_{k,F_k}^\tau$ , respectively, as defined in Equation 2.

$$\hat{y}_{g,F_k}^\tau = \sum_{i \in F_k} (\hat{y}_g^\tau)_i \quad \text{and} \quad \hat{y}_{k,F_k}^\tau = \sum_{i \in F_k} (\hat{y}_k^\tau)_i \quad (2)$$

This grouping technique produces a new probability distribution that encapsulates an accumulated probability for all classes in  $F_k$  alongside the probabilities for each background class. However, directly applying this formulation to the loss function introduces conflicts in the optimization target. Specifically, since the probabilities of the labeled organs in  $\hat{y}_g^\tau$  cannot be perfectly aligned with the ground truth  $y_k$ , this discrepancy may lead to ambiguous or even erroneous optimization objectives, ultimately degrading the segmentation performance. This conflict will be addressed later in Section 3.4.3 through the use of conditional probability techniques.

#### 3.4.2 Background Class Grouping

In medical image segmentation, lesion regions are often small and vary significantly in size, shape, and location.

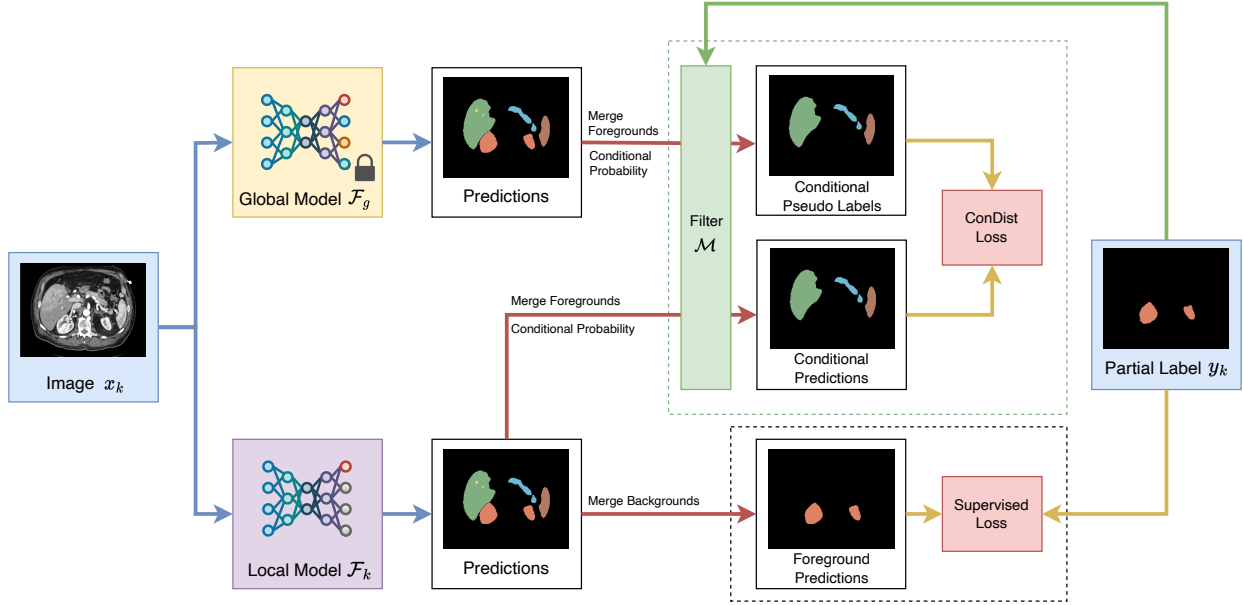


Figure 2: Illustration of the ConDistFL client training process on a partially labeled dataset, where only the kidney and kidney tumor are annotated. The model is trained to leverage both local and global knowledge for effective segmentation of labeled and unlabeled organs.

To reduce the risk of inaccurate lesion predictions from the global model, we group unlabeled organs together with their respective tumors. This grouping technique increases tolerance for erroneous lesion prediction by reformulating the lesion segmentation problem to an organ segmentation problem. Let  $M_k$  denote the number of unlabeled organs in client  $k$ , and  $\mathcal{O}_k = \{G_0, G_1, \dots, G_{M_k}\}$  where  $G_0 = \{0\}$  is the set including the background class, and  $G_i$  is the set including the class index of  $i$ -th organ and all classes of its anomaly areas for  $i=1, 2, \dots, M_k$ . By accumulating the probabilities of each group  $G_i$ , we can define  $\hat{y}_{g, G_i}^T$  and  $\hat{y}_{k, G_i}^T$  as follow:

$$\hat{y}_{g, G_i}^T = \sum_{j \in G_i} (\hat{y}_g^T)_j \quad \text{and} \quad \hat{y}_{k, G_i}^T = \sum_{j \in G_i} (\hat{y}_k^T)_j \quad (3)$$

Additionally, due to the lack of diagnostic confirmation for the predicted lesion areas, the true nature of these lesions remains uncertain. This grouping technique helps to address the issue of misidentification.

### 3.4.3 Conditional Probability

The ConDist loss employs conditional probability to prevent interference between the supervised loss and the ConDist loss. This technique is essential for resolving the conflicts between  $y_k$  and  $\hat{y}_g^T$  discussed in Section 3.4.1. By assuming that the given probability is a class in  $B_k$ , we can calculate the conditional probabilities  $\hat{y}_{g, \mathcal{O}_k | B_k}^T$  and  $\hat{y}_{k, \mathcal{O}_k | B_k}^T$  using the following equation:

$$\hat{y}_{g, \mathcal{O}_k | B_k}^T = \left( \frac{\hat{y}_{g, G_0}^T}{1 - \hat{y}_{g, F_k}^T}, \frac{\hat{y}_{g, G_1}^T}{1 - \hat{y}_{g, F_k}^T}, \dots, \frac{\hat{y}_{g, G_{M_k}}^T}{1 - \hat{y}_{g, F_k}^T} \right), \quad (4)$$

$$\hat{y}_{k, \mathcal{O}_k | B_k}^T = \left( \frac{\hat{y}_{k, G_0}^T}{1 - \hat{y}_{k, F_k}^T}, \frac{\hat{y}_{k, G_1}^T}{1 - \hat{y}_{k, F_k}^T}, \dots, \frac{\hat{y}_{k, G_{M_k}}^T}{1 - \hat{y}_{k, F_k}^T} \right), \quad (5)$$

This conditional probability formulation ensures that  $\hat{y}_{g, \mathcal{O}_k | B_k}^T$  and  $\hat{y}_{k, \mathcal{O}_k | B_k}^T$  are independent of any foreground classes in  $F_k$ . By isolating the background classes in this conditional probability formulation, the ConDist

loss can effectively minimize errors related to unlabeled classes without affecting the supervised learning process.

### 3.4.4 Foreground Filtering

Foreground filtering is a crucial technique for improving the accuracy of pseudo-labels in distillation learning for unlabeled classes. Since human organs do not overlap, incorrect segmentation of foreground classes  $F_k$  in the global model’s prediction  $\hat{y}_g^T$  can be identified using the partial ground truth labels  $y_k$ . To leverage this characteristic and improve segmentation performance, we introduce a binary mask  $\mathcal{M}$  for foreground filtering. This mask shares the spatial shape of the ground truth labels  $y_k$  and is defined in equation 6 as follows:

$$\mathcal{M} = \begin{cases} 0 & (\operatorname{argmax}_i(\hat{y}_g^T)_i \in F_k) \vee (\operatorname{argmax}_i(y_k)_i \in F_k) \\ 1 & \text{Otherwise} \end{cases} \quad (6)$$

The mask  $\mathcal{M}$  is applied via element-wise multiplication to both  $\hat{y}_{g, \mathcal{O}_k|B_k}^T$  and  $\hat{y}_{k, \mathcal{O}_k|B_k}^T$  to exclude foreground regions.

The binary mask  $\mathcal{M}$  ensures the effectiveness of the distillation process by filtering out irrelevant or incorrectly predicted areas. Specifically, it excludes regions corresponding to labeled classes in  $F_k$ , including correctly segmented, under-segmented, and over-segmented areas. In correctly segmented regions, the probabilities of the unlabeled classes are irrelevant due to the availability of ground truth labels; hence, these regions are filtered out and handled by the supervised loss. For incorrectly segmented areas—whether under-segmented or over-segmented—the mask discards the global model’s erroneous predictions, preventing the local model from learning inaccurate information. Moreover, the mask helps mitigate numerical instability during loss calculation by ensuring the denominator in equation 4 does not approach zero.

### 3.4.5 ConDist Loss for Segmentation

In our proposed conditional distillation, we aim to minimize the distance between  $\hat{y}_{k, \mathcal{O}_k|B_k}^T$  and  $\hat{y}_{g, \mathcal{O}_k|B_k}^T$ . In the context of segmentation, the soft Dice loss  $\mathcal{L}_{Dice}$  is a popular option for knowledge distillation because the Dice score is the primary metric for evaluating

model performance. By combining the foreground filter  $\mathcal{M}$  and the soft Dice loss, we define the ConDist loss  $\mathcal{L}_{ConDist}$  in equation 7 as follows:

$$\mathcal{L}_{ConDist} = \mathcal{L}_{Dice}(\mathcal{M} \cdot \hat{y}_{k, \mathcal{O}_k|B_k}, \mathcal{M} \cdot \hat{y}_{g, \mathcal{O}_k|B_k}) \quad (7)$$

## 3.5 Combining Supervised and ConDist Losses

The total loss function  $\mathcal{L}_{total}$ , as defined in Equation 8, combines the supervised loss  $\mathcal{L}_{sup}$  and the ConDist loss  $\mathcal{L}_{ConDist}$ . A weighting parameter  $\lambda$  is introduced to adjust the influence of the ConDist loss during training. This parameter is initialized with a small value and increased linearly throughout training to allow the global model to stabilize before its knowledge is used more heavily in local training.

$$\mathcal{L}_{total} = \mathcal{L}_{sup} + \lambda \mathcal{L}_{ConDist} \quad (8)$$

By incrementally increasing  $\lambda$ , we ensure that the model gradually incorporates global knowledge while still prioritizing the available local labels in early FL rounds.

## 4 Experiments

### 4.1 Experiment Settings

In this study, we comprehensively evaluated our proposed method on both 3D abdominal CT segmentation and 2D chest X-ray segmentation tasks. For the 3D abdominal CT segmentation, we utilized five distinct datasets: four in-federation datasets (MSD (Antonelli et al., 2021) Liver, MSD Pancreas, MSD Spleen, and KiTS19 (Heller et al., 2021)) and one out-of-federation dataset (AMOS22 (Ji et al., 2022)). The in-federation MSD datasets were used for training, validation, and testing phases to robustly assess model performance. Specifically, the MSD Liver dataset, consisting of contrast-enhanced CT images, provided annotations for the liver and associated tumors, while the MSD Pancreas dataset focused on the pancreas and pancreatic tumors, with images acquired in the portal venous phase. Similarly, the MSD Spleen dataset targeted spleen segmentation in the portal venous phase images. The KiTS19 dataset provided

kidney and kidney tumor annotations, utilizing arterial phase imaging. The AMOS22 dataset, reserved solely for testing, includes a broader array of labels for 15 organs, including the kidney, liver, pancreas, and spleen, evaluated under varied contrast conditions (including non-contrast phase images). The detailed data splits for training, validation, and testing are presented in Table 2.

For the 3D segmentation tasks, we employed the MedNeXt-Base (Roy et al., 2023b) architecture, a state-of-the-art model for 3D CT segmentation. The training configurations included a voxel spacing of 1.5 mm in each dimension to ensure effective spatial resolution. The intensity range of the CT images was standardized between  $-54$  and  $258$ , with normalization performed using a mean of  $100$  and a standard deviation of  $50$ . The input volume was shaped to  $128 \times 128 \times 128$  voxels, balancing computational efficiency and spatial detail. The model was trained with an initial learning rate of  $10^{-3}$  using the AdamW optimizer, and the learning rate was adjusted with a cosine annealing schedule over 120,000 steps.

In the 2D chest X-ray experiments, we employed four in-federation datasets: Montgomery (Jaeger et al., 2014b; Candemir et al., 2014), Shenzhen (Jaeger et al., 2014a; Rajaraman et al., 2021), JSRT (Shiraishi et al., 2000), and SIIM-ACR (Zawacki et al., 2019). Both the Montgomery and Shenzhen datasets provided annotations for the left and right lungs, with the right lung label reserved for testing in the Montgomery dataset and the left lung label used exclusively for testing in the Shenzhen dataset. The JSRT dataset included annotations for the left lung, right lung, and heart, with the lung annotations utilized for testing. The SIIM-ACR dataset, comprising 12,047 images, focused on pneumothorax detection and contained both pneumothorax and non-pneumothorax cases. Pneumothorax images were annotated with masks indicating the affected area, whereas non-pneumothorax images had empty masks. The SIIM-ACR dataset had a pneumothorax to non-pneumothorax ratio of 2,669:9,378. This ratio was preserved during the dataset split, resulting in 1,600 pneumothorax images in the training set, 534 in the validation set, and 535 in the test set. Detailed data splits are provided in Table 3.

For 2D segmentation tasks, we employed the DeepLabV3+ (Chen et al., 2017) architecture with a ConvNeXtV2-Tiny (Woo et al., 2023) encoder, pre-trained on the ImageNet dataset to enhance feature

extraction. An additional binary classification head was added to the encoder for pneumothorax detection. The input images were resized to  $512 \times 512$  pixels and normalized using z-score normalization. The model was trained with an initial learning rate of  $10^{-4}$  using the AdamW optimizer, and the learning rate was adjusted following a cosine annealing strategy over 15,000 steps to ensure convergence.

## 4.2 FL Configurations

To evaluate our proposed method under federated learning conditions, we implemented a horizontal FL setup comprising one server and four clients, simulating real-world scenarios. For the 3D CT experiments, the KiTS19 and MSD datasets were distributed among the four clients, while for the 2D X-ray experiments, the Montgomery, Shenzhen, JSRT, and SIIM-ACR datasets were assigned to the clients. Each client was equipped with an NVIDIA V100 GPU, and local training was conducted in parallel across all clients. The implementation was based on PyTorch (Ansel et al., 2024), NVFLare (Roth et al., 2023), and MONAI (Jorge Cardoso et al., 2022) for both 2D and 3D medical image processing.

We conducted a comprehensive evaluation of ConDistFL, comparing it with traditional FL methods (FedAvg (McMahan et al., 2017), FedProx (Li et al., 2020), and FedOpt (Reddi et al., 2020)) on both 2D and 3D segmentation tasks. Additionally, for the 3D segmentation tasks, we compared ConDistFL with Kim et al.’s (Kim et al., 2024) method, as it shares similarities with our approach by employing a 3D segmentation model and knowledge distillation during training.

In all FL experiments, except for FedOpt, the server employed the FedAvg aggregation algorithm with equal weighting for each client. For FedOpt experiments, the server-side aggregation was performed using an SGD optimizer with a learning rate of 1.0 and a momentum of 0.6 to ensure efficient weight aggregation.

In the experiments involving FedAvg, FedProx, FedOpt, and ConDistFL, all clients adhere to the training configurations detailed in Section 4.1. For the FedAvg, FedProx, and FedOpt experiments, the loss function was the marginal Dice loss combined with cross-entropy, as described in Section 3.3. In the case of ConDistFL, the supervised loss was complemented by the ConDist loss,



Table 2: Overview of 3D CT datasets used in experiments. The AMOS22 dataset annotates the whole organ, regardless of whether the organ is healthy or not.

Dataset	Data Split			Annotations							
	Training	Validation	Test	Kidney	Kidney Tumor	Liver	Liver Tumor	Pancreas	Pancreas Tumor	Spleen	
KiTS19	126	42	42	✓	✓						
MSD Liver	79	26	26			✓	✓				
MSD Pancreas	169	56	56					✓	✓		
MSD Spleen	25	8	8							✓	
AMOS22	0	0	300	✓		✓		✓		✓	

Table 3: Data split and annotation information for each Dataset used in 2D chest X-ray experiments.

Dataset	Data Split			Annotations			
	Training	Validation	Test	Left Lung	Right Lung	Heart	Pneumothorax
Montgomery	82	27	29	✓	✓		
Shenzhen	232	77	79	✓	✓		
JSRT	147	49	50	✓	✓	✓	
SIIM-ACR	7,226	2,410	2,411				✓

as defined in Equation 8. For the 3D experiments, the FL aggregation process was set to 120 rounds, with each client optimizing its local model for 1,000 steps per round using its partially labeled dataset. For the 2D experiments, the FL process was set to 30 rounds, with each client optimizing its local model for 500 steps per round.

In the FedProx experiments, the proximal term parameter was set to  $\mu = 10^{-6}$ . For ConDistFL, the temperature parameter  $\tau$  was fixed at 0.5, while the loss weight  $\lambda$  was gradually increased from 0.01 to 1.0 throughout the training rounds. In implementing Kim et al.’s method, we adopted their proposed 3D U-Net architecture with organ-specific segmentation heads using the specified training configurations. Kim et al.’s approach was distinct in that it utilized 1,000 FL rounds, with each client performing 80 steps per round.

We employed two strategies to ensure optimal model selection during FL training. The global model was evaluated at the start of each round, with the best model selected based on the highest average Dice score across all clients’ validation sets. Conversely, local models were evaluated at the end of each round, with the best local models selected based on the highest average Dice score on their respective client’s validation set.

## 5 Results

In this section, we present a comprehensive evaluation of ConDistFL compared to existing federated learning methods. The analysis includes quantitative results, visualizations, and an ablation study to assess the impact of specific techniques. We evaluated the segmentation performance of ConDistFL and other methods using in-federation test sets from 3D abdominal CT and 2D chest X-ray datasets. Additionally, to assess generalizability, we employed the out-of-federation dataset AMOS22 and evaluated the performance of the best FL global models. The primary evaluation metric for all experiments is the Dice score.

### 5.1 Quantitative Evaluation

Table 4 and 5 present the test results for the 3D abdominal CT and 2D chest X-ray experiments conducted on the in-federation test set. The performance metrics for FL methods are based on the best-performing global models, while the standalone results are derived from an ensemble of models trained individually on each client’s private dataset without federated learning.

Table 4: In-Federation Test Dice Scores for ConDistFL and Comparative Methods. This table compares Dice scores for various organs and lesions across the standalone model and federated learning methods. ConDistFL consistently achieves the highest average Dice score, indicating superior segmentation performance.

Method	Average Dice $\uparrow$	Kidney		Liver		Pancreas		Spleen
		Organ	Tumor	Organ	Tumor	Organ	Tumor	Organ
Standalone	0.8167	<b>0.9563</b>	0.8116	0.9520	0.7265	0.7846	0.5126	0.9631
FedAvg	0.8091	0.9536	0.7766	0.9608	0.7241	0.7824	0.5041	0.9618
FedProx	0.7432	0.7736	0.7481	0.8973	0.5968	0.7893	0.5049	0.8923
FedOpt	0.7598	0.6767	0.7751	0.8915	0.6908	0.7841	<b>0.5435</b>	0.9568
Kim et al.	0.7330	0.9430	0.6734	0.9386	0.6439	0.7207	0.3778	0.8334
ConDistFL (ours)	<b>0.8235</b>	0.9547	<b>0.8247</b>	<b>0.9613</b>	<b>0.7322</b>	<b>0.7975</b>	0.5278	<b>0.9664</b>

Table 5: In-Federation Test Dice Scores for 2D Chest X-Ray Experiments. L. denotes the left side, and R. denotes the right side of the organ. Organs marked with an asterisk (\*) had their segmentation masks excluded from training and validation, and were used only for testing.

Method	Average Dice $\uparrow$		Montgomery		Shenzhen		JSRT		SIIM-ACR	
	Exclude*	Include*	L. Lung	R. Lung*	L. Lung*	R. Lung	L. Lung*	R. Lung*	Heart	Pneumothorax
Standalone	0.9299	0.9456	<b>0.9809</b>	0.9544	0.9565	0.9699	0.9626	0.9715	<b>0.9544</b>	0.8146
FedAvg	0.9147	0.8281	0.9731	0.6689	0.5236	0.9641	0.9137	0.8601	0.9242	0.7974
FedProx	0.9280	0.7536	0.9791	0.4367	0.5032	0.9663	0.8432	0.5338	0.9426	0.8240
FedOpt	0.8354	0.7614	0.6984	0.8238	0.4837	0.9348	0.6251	0.8173	0.9052	0.8033
ConDistFL (ours)	<b>0.9325</b>	<b>0.9489</b>	0.9803	<b>0.9674</b>	<b>0.9577</b>	<b>0.9702</b>	<b>0.9630</b>	<b>0.9728</b>	0.9537	<b>0.8258</b>

As shown in Table 4, ConDistFL consistently achieves the highest average Dice scores across multiple organ and tumor classes, including kidney tumor, liver, liver tumor, pancreas, and spleen. This performance surpasses standalone models and other FL methods, highlighting ConDistFL’s robustness and effectiveness in diverse segmentation tasks. Notably, ConDistFL attains the best overall average Dice score across all seven classes. This is particularly significant in comparison to the sharp drops in Dice scores observed for kidney tumors in competitive FL methods when compared to standalone models. Additionally, FedProx, FedOpt, and Kim et al.’s methods exhibit considerable performance gaps in liver tumor segmentation, further contributing to their lower efficacy. Kim et al.’s method, in particular, shows significant drops in performance for pancreas tumor and spleen segmentation, resulting in the lowest overall average Dice score. In contrast, ConDistFL effectively mitigates these performance losses, particularly excelling

in challenging cases such as kidney and liver tumor segmentation, surpassing the standalone baseline.

Table 5 presents the results of the 2D chest X-ray segmentation experiments. For the lungs and heart segmentation tasks, the Dice score calculation excludes empty labels, meaning that only non-empty predictions are considered when evaluating performance for these classes. Regarding pneumothorax segmentation, we follow the SIIM-ACR Pneumothorax Segmentation Challenge (Zawacki et al., 2019) guidelines for Dice score calculation. This approach assigns a Dice score of 1.0 for correctly predicted empty segmentation masks in non-pneumothorax cases and 0.0 for incorrect non-empty predictions, ensuring that the evaluation accurately reflects the model’s ability to detect pneumothorax.

Table 5 also highlights ConDistFL’s strong performance in 2D chest X-ray segmentation, where it achieves the highest average Dice scores across most categories, except for the left lung in the Montgomery dataset and

Table 6: Training time and data traffic for 3D abdominal CT segmentation using different federated learning methods. Note: Pre-training time for local teacher models in Kim et al. is excluded.

Method	#Rounds	Model Size	Traffic Size	Training Time
FedAvg	120	40.6 MB	38.0 GB	93.0 h
FedProx	120	40.6 MB	38.0 GB	95.0 h
FedOpt	120	40.6 MB	38.0 GB	94.7 h
Kim et al.	1000	60.4 MB	471.6 GB	119.1 h
ConDistFL (Ours)	120	40.6 MB	38.0 GB	102.5 h

Table 7: Training time and data traffic size for 2D chest X-ray segmentation using different FL methods.

Method	#Rounds	Model Size	Traffic Size	Training Time
FedAvg	30	336.3 MB	78.8 GB	5.2 h
FedProx	30	336.3 MB	78.8 GB	5.3 h
FedOpt	30	336.3 MB	78.8 GB	5.2 h
ConDistFL (Ours)	30	336.3 MB	78.8 GB	5.9 h

the heart in the JSRT dataset. Notably, ConDistFL performs better than the standalone models for test-only labels on Montgomery, Shenzhen, and JSRT datasets. In contrast, the right lung Dice scores in the Montgomery dataset and the left lung Dice scores in the Shenzhen dataset show a significant decline in FedAvg, FedProx, and FedOpt models compared to standalone models, further underscoring the effectiveness of ConDistFL.

## 5.2 FL Computation and Communication Efficiency

The computational and communication efficiency of ConDistFL and other FL methods are compared in Tables 6 and 7. These tables summarize the total training time and data traffic size for 3D abdominal CT and 2D chest X-ray segmentation tasks. The total data traffic size is calculated as  $2 \times (\text{number of rounds}) \times (\text{number of clients}) \times (\text{model size})$ , where the factor of 2 accounts for both sending and receiving model updates between the clients and the central server.

In the 3D abdominal CT experiments (Table 6), ConDistFL demonstrates efficient communication and computation. The total data traffic for ConDistFL is 38.0 GB, which is identical to traditional FL methods like FedAvg, FedProx, and FedOpt, as it uses the same

number of rounds and model sizes. The training time for ConDistFL is 102.5 hours, only marginally longer than FedAvg (93.0 hours), FedProx (95.0 hours), and FedOpt (94.7 hours). This slight increase is due to the additional computation introduced by the conditional distillation process, but it remains a manageable overhead.

Compared to Kim et al.’s method, ConDistFL is both more communication and computationally efficient. The reduced communication overhead in ConDistFL is due to using fewer FL rounds and a smaller model with fewer parameters. ConDistFL also achieves a shorter training time, as it relies solely on the global model for knowledge distillation, whereas Kim et al.’s approach incorporates both the global model and multiple pre-trained local teacher models, increasing computational demands. Furthermore, the training time reported for Kim et al.’s method does not include the pre-training phase for the teacher models, which would further add to the overall computational cost.

For the 2D chest X-ray experiments (Table 7), ConDistFL maintains the same level of communication efficiency as FedAvg, FedProx, and FedOpt, with a total traffic size of 78.8 GB. The training time for ConDistFL (5.9 hours) is slightly longer than FedAvg (5.2 hours), FedProx (5.3 hours), and FedOpt (5.2 hours), which is expected due to the added computation for conditional distillation.

In summary, ConDistFL achieves a good balance between computation and communication efficiency, offering competitive performance without increasing communication costs. The slight increase in training time is a reasonable trade-off for the enhanced segmentation performance, especially when compared to methods that require much larger communication bandwidth and more extensive training time.

## 5.3 Dice Score Distribution Analysis

Figure 3 illustrates the distribution of test Dice scores for the global models and the best local models from each client on the in-federation test set for the 3D abdominal CT experiments. The global models across all FL methods demonstrate reasonable performance across all classes, as reflected in the metrics presented in Table 4.

Examining the local models, particularly for healthy organ segmentation, ConDistFL shows a consistent performance between its local models and global model,

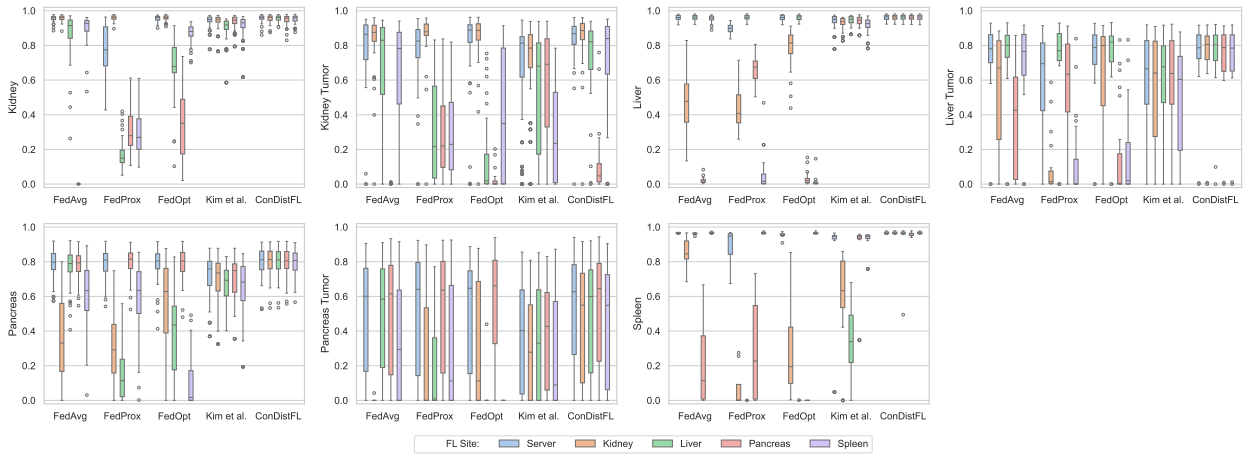


Figure 3: Boxplot of test Dice score distributions for global models trained using different federated learning methods on the in-federation test set from the 3D abdominal CT experiments. The Dice scores represent the segmentation performance across multiple clients, with higher scores indicating better agreement between predicted and ground-truth segmentations.

with minimal variation in Dice scores. A similar pattern is observed in Kim et al.’s method, where the local models perform comparably to the global model for kidney, liver, and pancreas segmentation. However, two clients in Kim et al.’s method exhibit severe performance drops in spleen segmentation. In contrast, traditional FL methods, including FedAvg, FedProx, and FedOpt, display significant performance degradation in at least one client for each organ, with some local models nearly failing to segment specific organs (indicated by median Dice scores close to 0.0).

When analyzing tumor segmentation, ConDistFL maintains consistent performance across kidney and pancreas tumors, with similar median Dice scores across local models. However, the pancreas local model shows a notable exception, with a median Dice score below 0.2 for the kidney tumor. Kim et al.’s method similarly demonstrates stable performance across most tumor classes, with consistent median Dice scores between the global and local models for liver, kidney, and pancreas tumors. An exception is found in the spleen client, where the local model exhibits a significant drop in kidney and pancreas tumor segmentation. Traditional FL methods show more pronounced inconsistencies, with significant

performance drops in tumor segmentation. For example, one FedAvg local model shows a sharp decline in liver tumor segmentation, and two clients from FedProx and FedOpt fail to segment the liver tumor. Additionally, in pancreas tumor segmentation, the FedAvg kidney local model fails, while FedProx and FedOpt each have two local models that fail to segment the pancreas tumor.

Figure 4 shows the Dice score distribution for global and local models in our 2D experiment on the in-federation test set. We first focus on the Dice scores for the labels used during training: the left lung in the Montgomery dataset, the right lung in the Shenzhen dataset, the heart in the JSRT dataset, and pneumothorax in the SIIM-ACR dataset.

For the left lung (Montgomery), right lung (Shenzhen), and heart (JSRT), ConDistFL consistently maintains strong performance, with only one local model showing a significant drop in Dice score compared to the global model and other clients. In contrast, other methods have at least two clients with noticeable declines in Dice scores.

Regarding to the pneumothorax class in the SIIM-ACR dataset, Figure 4 focuses on the 535 images labeled as pneumothorax to assess the segmentation ability of each model. The results demonstrate that the SIIM-

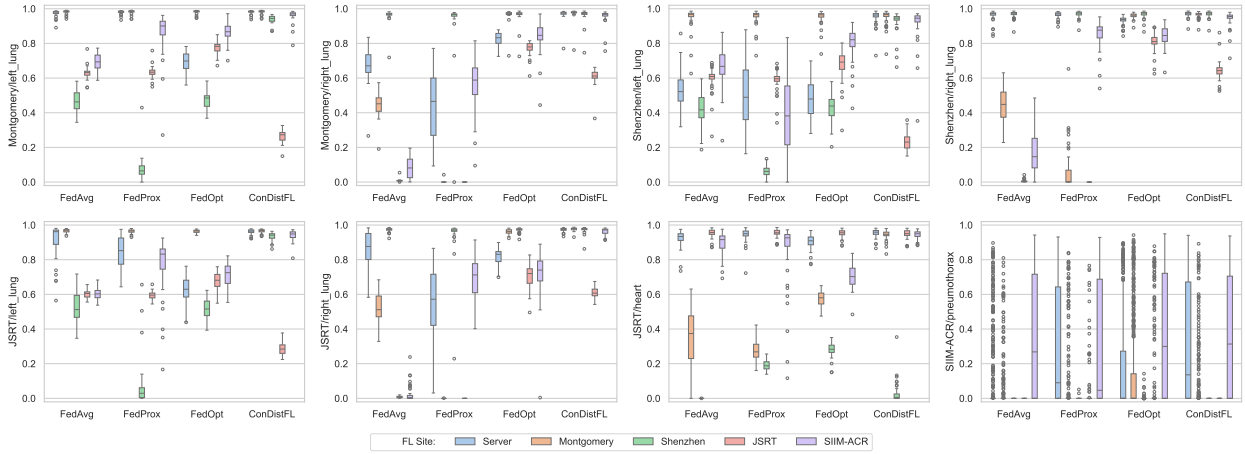


Figure 4: Boxplot of test Dice score distributions for global models trained using different federated learning methods on the in-federation test set from the 2D chest X-ray experiments. For the pneumothorax segmentation, the boxplot excludes non-pneumothorax images, displaying only the Dice scores for pneumothorax cases.

ACR local model trained using ConDistFL achieves the highest median Dice score among all local models, while the ConDistFL global model also outperforms other global models with the highest median Dice score. Across all evaluated FL methods, only the SIIM-ACR local model effectively segments the pneumothorax areas, with most other local models failing to produce accurate segmentations. Notably, only the Montgomery client’s local model in FedOpt manages to achieve a non-zero 75th percentile Dice score for pneumothorax segmentation.

Next, we examine the test-only labels in the Montgomery, Shenzhen, and JSRT datasets. For the right lung in the Montgomery and JSRT datasets, both the global model and all local models of ConDistFL exhibit consistently high performance, except for the JSRT client, where the median Dice score drops significantly to just above 0.6. In contrast, under FedAvg, the median Dice scores of local models from Montgomery, JSRT, and SIIM-ACR clients drop below 0.6, with the JSRT local model showing an almost zero median Dice score. Additionally, the FedAvg global model demonstrates a lower median Dice score than its local model from the Shenzhen client. FedProx shows a similar but more severe trend, with the global model’s median Dice score significantly lower than that of FedAvg, and the local models

for Montgomery and JSRT showing median Dice scores close to 0.0 for the right lung in both the Montgomery and JSRT clients. For FedOpt, the variation in median Dice scores between the global model and each client is less pronounced compared to FedAvg and FedProx; however, the median Dice scores for the global model and the JSRT and SIIM-ACR local models hover around 0.8.

For the left lung label in the Shenzhen and JSRT datasets, both the global model and all local models maintain consistently high performance except for the JSRT local model. However, the JSRT client’s median Dice score drops to just above 0.2. In the cases of FedAvg, FedProx, and FedOpt, only the Montgomery clients and the FedAvg global model achieve high median Dice scores (close to 1.0). For the other models, median Dice scores typically range between 0.4 and 0.8, with the Shenzhen local model under FedProx showing a particularly low median Dice score, dropping below 0.1.

In summary, the Dice score distributions for both 3D and 2D test sets across all FL sites reveal that ConDistFL’s local models exhibit Dice score distributions consistent with its global model. In contrast, for other methods, while the global model may achieve high median Dice scores, the local models often struggle, with median Dice scores for certain classes falling to around 0.0, indicating

Table 8: Out-of-Federation test Dice scores on AMOS22 Dataset for 3D abdominal CT experiments.

Method	Average	Kidney	Liver	Pancreas	Spleen
Standalone	0.7055	0.7063	0.6406	0.5805	0.8947
FedAvg	0.6721	0.4598	0.8314	0.5456	0.8516
FedProx	0.5965	0.4020	0.8073	0.5466	0.6302
FedOpt	0.5362	0.1805	0.7303	0.4852	0.7487
Kim et al.	0.6972	0.5738	0.9166	0.6116	0.6867
ConDistFL (ours)	<b>0.8635</b>	<b>0.9068</b>	<b>0.9318</b>	<b>0.6919</b>	<b>0.9235</b>

a failure to segment those classes effectively.

## 5.4 Generalizability on Out-of-Federation Dataset

We present the test results of our 3D abdominal experiments on the out-of-federation test set, AMOS22, in Table 8. The AMOS22 dataset consists of multi-phase CT images from individuals with non-specific abdominal diseases. Notably, anomalies in these images are not separately annotated from the organs, and the dataset does not specify the types of diseases present. As a result, when computing the Dice scores for this out-of-federation test, we grouped organ predictions with their associated lesion predictions (e.g., kidneys with kidney tumors) to align with the label definitions provided in the AMOS22 dataset.

As demonstrated in Table 8, ConDistFL exhibits superior performance compared to both standalone models and other federated learning methods, highlighting its enhanced generalizability. While Kim et al.’s method records the lowest average Dice score on the in-federation test set, it outperforms FedAvg, FedProx, and FedOpt on the out-of-federation test set. It surpasses the standalone model in the liver and pancreas classes. Additionally, all competitive methods, including FedAvg, FedProx, FedOpt, and Kim et al., experience significant performance degradation in the kidney class. Among them, Kim et al.’s method maintains a relatively stable average Dice score of 0.5738, which, although lower than the standalone model’s 0.7063, remains substantially higher than the Dice scores of traditional FL methods.

## 5.5 Ablation Study

Table 9 presents the results of the ablation study on the ConDist loss, focusing on the out-of-federation test set. The experiment incorporating background grouping and foreground filtering techniques achieved the highest average Dice score, demonstrating the effectiveness of combining these approaches.

Table 9: Ablation study on ConDistFL with background class grouping and foreground filtering on the out-of-federation AMOS22 dataset.

Group	Filter	Average	Kidney	Liver	Pancreas	Spleen
		0.8375	0.8952	0.8687	<b>0.6981</b>	0.8881
✓		0.8454	0.9063	0.9020	0.6681	0.9052
	✓	0.8361	0.8975	0.8965	0.6496	0.9007
✓	✓	<b>0.8635</b>	<b>0.9068</b>	<b>0.9318</b>	0.6919	<b>0.9235</b>

For the in-federation test, the ablation study results show that ConDistFL, without either grouping or filtering techniques, achieved an average Dice score of 0.8202 across the 7 classes. Introducing background grouping alone improved the average score to 0.8293 while using only foreground filtering resulted in a score of 0.8199. Compared to the ConDistFL version with both grouping and filtering, which achieved an average Dice score of 0.8235 (as shown in Table 4), the configuration with grouping alone yielded the highest score, though the improvement was marginal.

However, the ablation study on the out-of-federation test set reveals that employing both grouping and filtering significantly enhances generalizability, particularly for the kidney, liver, and spleen classes. While using either technique alone improves the average Dice scores for these organs, they have an opposing effect on the Dice score of the pancreas class. When both techniques are combined, the Dice scores for the kidney, liver, and spleen further improve compared to using just one of these methods. Moreover, the reduction in pancreas Dice scores is significantly mitigated when both grouping and filtering are applied together, compared to the version without either technique.

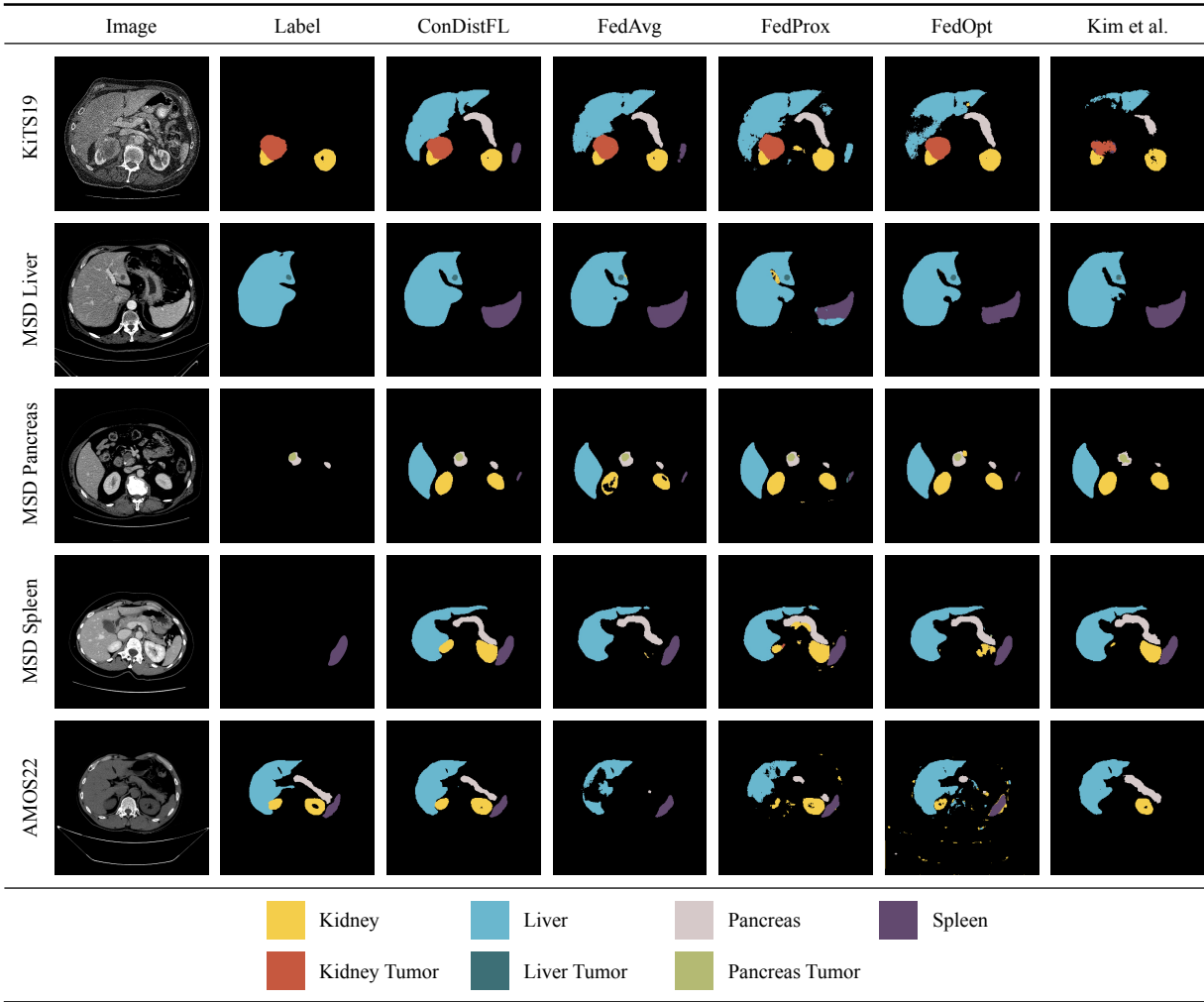


Figure 5: Visual comparison of segmentation results from ConDistFL, FedAvg, FedProx, FedOpt, and Kim et al. on representative slices from the in-federation 3D CT test set. The figure shows the original images, ground truth labels, and predicted segmentations. ConDistFL demonstrates more accurate and consistent segmentation across various organs than other methods.

## 5.6 Visualization of Segmentation Results

Figures 5 and 6 illustrate the segmentation results of the FL global models for the 3D and 2D experiments conducted on the test sets.

Figure 5 presents CT images showcasing the per-

formance of each method under various conditions, including different contrast phases, abdominal positions, and image qualities. Images from the MSD dataset exhibit high clarity and well-defined edges, facilitating accurate segmentation. In contrast, the KiTS19 image displays lower quality, with increased noise and reduced contrast, although the abdominal structure edges

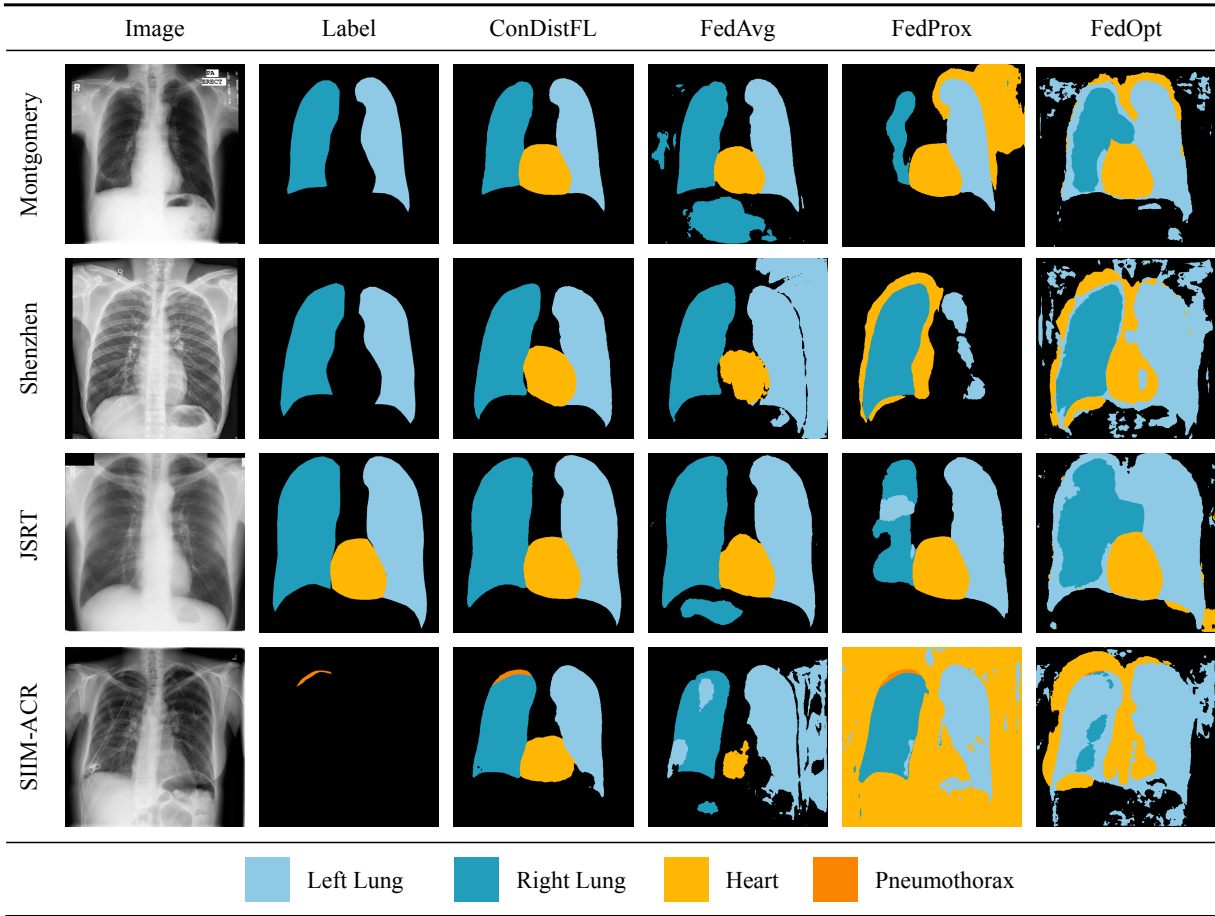


Figure 6: Visual comparison of segmentation results from ConDistFL, FedAvg, FedProx, and FedOpt on representative images from the in-federation 2D chest X-ray test set. The figure shows the original X-ray images, ground truth labels, and predicted segmentations. ConDistFL provides more precise and consistent segmentations for both lung and pneumothorax regions than other methods.

remain sufficiently clear to enable accurate segmentation. The AMOS22 image, being non-contrast CT, has a significantly different intensity distribution compared to the other datasets, and the edges of abdominal structures are less distinct, making segmentation more challenging.

For the in-federation datasets, all FL methods generally perform well on labeled organs, producing segmentations without major errors. However, performance differences become more evident when

segmenting unlabeled organs. In the KiTS19 image, both ConDistFL and FedAvg successfully segment the liver, pancreas, and spleen, with ConDistFL achieving smoother and more complete segmentations. In contrast, FedProx, FedOpt, and Kim et al.’s method fails to segment the spleen accurately. FedProx mistakenly identifies the spleen as a part of the liver, while FedOpt and Kim et al.’s method exhibits incomplete liver segmentation with significant under-segmentation.



In the MSD Liver image, both ConDistFL and Kim et al.’s method accurately segment the liver, liver tumor, and spleen, although ConDistFL produces slightly more complete and smoother segmentations. FedProx, however, misidentifies parts of the spleen as liver tissue, and FedOpt fails to segment a portion of the spleen altogether. In the MSD Pancreas image, FedAvg produces incomplete kidney segmentations, leaving holes in both kidneys, while FedProx and FedOpt mislabel regions near the pancreas as kidney tissue.

For the MSD Spleen image, ConDistFL continues to demonstrate robust and consistent performance. While other FL methods successfully segment the liver, pancreas, and spleen, they exhibit significant under-segmentation of the kidneys. FedAvg performs particularly poorly in this regard, nearly failing to segment the kidney region, while FedProx mistakenly labels areas near the pancreas as kidney and generates false positives for kidney tumors.

In the AMOS22 image, ConDistFL is the only method that segments all four target organs without significant under-segmentation. Kim et al.’s method segments the liver and pancreas accurately but fails to segment the spleen and omits one kidney. For FedAvg, FedProx, and FedOpt, the spleen segmentation appears satisfactory, but severe mis-segmentation occurs for the remaining three organs.

Overall, ConDistFL consistently produces accurate and smooth segmentation of all target organs across the images in Figure 5. Although Kim et al.’s method shows less over-segmentation and improved smoothness compared to traditional FL methods, it fails to segment all target organs correctly in every image. Traditional FL methods like FedAvg and FedOpt perform well on labeled organs but struggle with unlabeled organs, often yielding less smooth segmentations than ConDistFL. FedProx, in particular, experiences difficulty distinguishing between the liver and spleen, leading to the poorest segmentation smoothness and the highest incidence of mis-segmented regions.

In Figure 6, the images from the Montgomery and Shenzhen datasets exhibit high quality, with clear visualization of the lungs and thoracic structures. The sharpness of lung and heart edges supports precise segmentation. The JSRT image is comparable in quality, though slight variations in contrast and patient

positioning result in a larger appearance of the heart. Conversely, the SIIM-ACR dataset images are of lower quality, with reduced contrast and sharpness, likely due to the clinical focus on pneumothorax detection, which may not require the same imaging clarity as general chest X-rays. The presence of pneumothorax also contributes to darker, less distinct regions in the images.

For the organs with labels used during training, the global models of ConDistFL, FedAvg, and FedProx generally produced reasonable segmentation results, though the FedAvg global model failed to segment pneumothorax, yielding an empty output. For the test-only labels in each dataset, ConDistFL accurately segmented the target organs without significant under-segmentation or over-segmentation. In contrast, FedAvg incorrectly included areas below the lungs as part of the right lung and misclassified background regions near the left lung as lung tissue. FedProx under-segmented the right lung in the Montgomery and JSRT images and under-segmented the left lung in the Shenzhen image. Additionally, the FedProx global model incorrectly identified areas around the right lung as the heart in the Shenzhen image and misclassified all areas outside the lungs as the heart in the SIIM-ACR image. The FedOpt model exhibited a tendency to mis-segment the right lung contour as part of the left lung and incorrectly marked random background areas as lung tissue. Similar issues were observed in heart segmentation, with background areas near the lungs being incorrectly labeled as heart tissue.

In the 2D experiments, the ConDistFL model consistently delivered accurate segmentations for both training-labeled and test-only organs, avoiding significant under-segmentation or over-segmentation issues. In contrast, the FedAvg model struggled with incorrect lung segmentations and failed to segment pneumothorax. The FedProx model frequently under-segmented lung areas and misidentified regions as heart tissue, particularly in the SIIM-ACR dataset. The FedOpt model exhibited mis-segmentation issues, incorrectly segmenting the lungs and heart areas. ConDistFL outperformed the other models, particularly in handling test-only labels with greater accuracy and consistency.

## 6 Discussion and Conclusion

This section discusses the key findings of our study, emphasizing the advantages of the ConDistFL method over other federated learning approaches. We highlight the importance of selecting an effective segmentation backbone, analyze the impact of the ConDist and marginal loss functions, evaluate ConDistFL’s generalizability in out-of-federation scenarios, and assess its computational efficiency and limitations. These insights collectively explain why ConDistFL outperforms both standalone models and competitive FL methods in medical image segmentation.

### 6.1 Impact of Backbones in Partially Labeled FL

In the context of partially labeled FL, the choice of model backbone plays a critical role in determining the segmentation performance. As demonstrated in Table 4, traditional FL methods such as FedAvg, FedProx, and FedOpt consistently achieve higher average Dice scores compared to Kim et al.’s method, even though Kim et al.’s approach is specifically designed for partial labeled FL scenarios. This discrepancy is largely attributed to the model backbones employed in the respective methods.

A key factor behind the superior performance of the traditional FL methods lies in their use of the state-of-the-art (SOTA) MedNeXt segmentation backbone. MedNeXt, as a more advanced and capable architecture, offers stronger feature extraction and representation capabilities, contributing to the higher Dice scores observed across multiple organ classes. In contrast, Kim et al.’s method relies on a customized 3D U-Net architecture with organ-specific segmentation heads. While this tailored approach may offer some advantages in handling partial labels, it does not deliver the same overall performance as the more powerful MedNeXt backbone.

The flexibility of our proposed ConDistFL method further underscores the importance of model backbone selection. Unlike Kim et al.’s approach, ConDistFL is architecture-agnostic and can be seamlessly integrated with any advanced segmentation backbone. By combining the SOTA MedNeXt model with our conditional distillation training framework, ConDistFL achieves superior segmentation performance, surpassing

competitive FL methods and standalone models. This adaptability allows ConDistFL to fully leverage the capabilities of the most recent and powerful architectures, further enhancing its effectiveness in multi-organ and tumor segmentation tasks.

The results in Table 4 clearly indicate that leveraging SOTA model architectures is essential for achieving optimal segmentation outcomes in partial labeled FL settings. ConDistFL’s architecture-agnostic design ensures that it can easily incorporate future advancements in segmentation backbones, making it a robust and scalable solution for medical image segmentation.

### 6.2 Analysis on Loss Functions

Our experimental results demonstrate that combining the marginal loss with the ConDist loss consistently outperforms setups that rely solely on the marginal loss, combine it with the FedProx proximal loss, or use cross-entropy-based knowledge distillation like in Kim et al.’s method (Kim et al., 2024). The ConDist loss offers three primary contributions to FL client training: (1) it mitigates catastrophic forgetting for unlabeled classes, (2) it provides a shared optimization target across clients, reducing model divergence, and (3) it resolves potential conflicts in optimization targets through its conditional probability design. These factors collectively improve convergence and higher Dice scores for global and local models.

A key aspect of preventing catastrophic forgetting during local client training is enabling the local model to retain knowledge of unlabeled organs by learning from the global model. This approach compensates for missing label information in partially labeled datasets, allowing the local model to maintain the knowledge gained during training and thereby preventing catastrophic forgetting. Both ConDistFL and Kim et al.’s method implement this strategy, and as shown in Figures 3 and 4, the local models in these methods exhibit Dice scores on unlabeled tasks that are closely aligned with their corresponding global models. This performance is in stark contrast to traditional FL methods, which do not specifically address catastrophic forgetting and consequently show larger discrepancies between their global and local models.

Model divergence is another significant challenge in federated learning, particularly in partially labeled setups where clients have different organ annotations. A com-

mon approach to mitigating model divergence is to provide a shared optimization target across clients, as seen in methods like FedProx. However, FedProx’s common optimization target is not task-specific and, as a result, is insufficient to address the divergence caused by inconsistent label distributions. This is evident in Figures 3 and 4, where FedProx’s global and local models exhibit high variation in performance, indicating persistent model divergence issues. In contrast, ConDistFL and Kim et al.’s method offers task-related common optimization targets that better align the local models with their global counterparts, leading to more consistent client behavior.

Addressing conflicts between loss functions is another critical issue in our setup, as ambiguous or conflicting optimization targets can prevent the model from converging to an optimal solution, ultimately degrading segmentation performance. ConDistFL resolves this issue by employing conditional probability in its knowledge distillation process, ensuring that the knowledge from the global model can be combined with incomplete labels without introducing conflicts. This design enables ConDistFL to achieve superior segmentation performance, as demonstrated in Tables 4 and 5, outperforming both traditional FL methods and ensembles of standalone models. This suggests that ConDistFL successfully leverages the benefits of federated learning to improve performance across diverse datasets.

In contrast, FedProx does not address the conflict between its optimization targets, which leads to overall poorer performance in its global model compared to FedAvg and FedOpt, both of which use marginal loss alone. Kim et al.’s method also suffers from conflicts during their knowledge distillation process. The conflict problem arises because Kim et al.’s method uses both the global model and multiple pre-trained teacher models for distillation, forcing the local model to fit multiple probability distributions. This issue is exacerbated by the fact that the pre-trained models are trained on individual datasets and are less effective when applied to unseen datasets from other clients, especially when those datasets differ in imaging characteristics (e.g., contrast phases). As a result, learning from inaccurate pseudo-labels generated by the pre-trained models degrades the overall segmentation performance.

In this section, we analyzed the effectiveness of the ConDist loss in federated learning, demonstrating how

it mitigates catastrophic forgetting, reduces model divergence, and resolves conflicts in optimization targets. Compared to alternative methods such as FedProx and Kim et al.’s knowledge distillation approach, ConDistFL provides a more robust and consistent training framework, leading to superior segmentation performance across global and local models. The careful design of ConDist loss ensures that learning from the global model is seamlessly integrated with partially labeled data while avoiding the issues that arise from conflicting loss terms.

### 6.3 Model Generalizability

ConDistFL demonstrates superior generalizability in out-of-federation tests, consistently surpassing both standalone models and other FL methods. This enhanced performance can be primarily attributed to two key factors: (1) the knowledge distillation process, which embeds information about unlabeled organs and enables the model to learn spatial relationships between different target organs within the same image, and (2) the improvement in pseudo-label quality through background grouping and foreground filtering techniques. Together, these elements allow ConDistFL to accurately segment target organs even in non-contrast CT images, as illustrated in Figure 5, despite the model being trained solely on contrast-enhanced CT images.

Knowledge distillation (KD) significantly enhances a model’s ability to understand spatial relationships between organs, thus improving its anatomical awareness in medical image segmentation. This advantage is evident when comparing KD-based methods like ConDistFL and Kim et al.’s approach with non-KD methods. As seen in Figure 5, non-KD methods often introduce random mis-segmentation or errors in irrelevant regions, whereas KD models avoid such mistakes and maintain correct spatial relationships between organs. For example, the FedProx model mis-segments the spleen as part of the liver in both the KiTS19 and MSD Liver images—errors not present in the KD models.

The improved segmentation quality of KD approaches can be attributed to their ability to incorporate anatomical information, while non-KD methods rely more on intensity-based features, which often lead to shape distortions and mis-segmentation. This distinction is further emphasized in Figure 6, where

non-KD methods fail to preserve the shape and spatial positioning of organs, while the ConDistFL model consistently produces more accurate segmentation.

Moreover, KD models exhibit greater robustness to intensity variations. In the AMOS22 non-contrast CT images, which represent an unseen phase during training, KD methods outperform non-KD models. The performance gains are evident in Figure 5 and Table 8, where KD approaches demonstrate superior generalizability and perform better on out-of-federation test sets than traditional FL methods. This enhanced generalizability underlines the importance of KD in improving segmentation performance in diverse imaging conditions.

The quality of pseudo-labels is critical for the effectiveness of knowledge distillation and directly impacts model generalizability. In our ablation study, ConDistFL, which incorporates background grouping and foreground filtering techniques to enhance pseudo-label quality, achieved the highest generalizability on the out-of-federation test set. These techniques ensure that pseudo-labels accurately represent unlabeled regions, enabling local models to better learn from the global model and preventing the propagation of incorrect information.

In contrast, Kim et al.’s approach, which uses both the global model and pre-trained teacher models for knowledge distillation, presents several challenges. As discussed in Section 6.2, this method introduces optimization conflicts between the loss functions and often degrades pseudo-label quality due to the reliance on pre-trained teacher models. Since these teacher models are trained on a single dataset, their predictions may not generalize well to unseen data from different distributions, leading to inaccurate pseudo-labels. Instead of enhancing generalizability, these errors can hinder it. As shown in Table 8, despite both methods using KD, ConDistFL significantly outperforms Kim et al.’s method on the out-of-federation test set. This highlights that high-quality pseudo-labels, like those generated in ConDistFL, are essential for achieving strong generalizability across diverse datasets.

In conclusion, ConDistFL’s superior generalizability stems from the combined benefits of knowledge distillation and high-quality pseudo-labels. The KD process enhances the model’s understanding of anatomical structures, while techniques like background grouping and foreground filtering ensure accurate pseudo-labels, mitigating the risk of error propagation. Together, these factors

significantly improve the model’s performance on out-of-federation test sets, making ConDistFL a robust and generalizable solution for medical image segmentation.

## 6.4 Efficiency and Computational Overhead

In real-world FL applications, both computational time and communication traffic between the server and clients are key considerations. As shown in Tables 6 and 7, ConDistFL incurs only a marginal increase in training time compared to traditional FL methods while maintaining a faster overall training time than Kim et al.’s method. In terms of communication traffic, ConDistFL matches traditional FL methods, as all these approaches share the same aggregation frequency. By contrast, Kim et al.’s method leads to significantly higher communication costs due to its more frequent aggregation rounds. These findings indicate that ConDistFL balances computational overhead and communication efficiency, offering high segmentation performance without imposing additional communication burdens, making it well-suited for real-world FL deployments.

The primary source of computational overhead in ConDistFL, compared to traditional FL methods, stems from the additional forward pass required by the global model during each training round. However, this extra computation constitutes only a small portion of the overall training time, largely dominated by the optimization steps. Our experimental results indicate that ConDistFL incurs a modest 10.2% increase in training time for 3D experiments and a 13.5% increase for 2D experiments compared to FedAvg. This marginal computational cost is offset by significant improvements in segmentation performance and generalizability, highlighting the method’s effectiveness in enhancing FL performance.

Communication traffic plays a crucial role in the overall performance of FL systems, particularly in bandwidth-limited environments. A key factor influencing traffic size is the number of aggregation rounds between the server and clients. Our results suggest that a lower number of aggregation rounds, combined with a higher number of local training steps per round, can achieve good performance. This contrasts with the settings used in other related works, such as MenuNet (Xu et al., 2023), which employs 400

rounds with one epoch of local training per round, and FedIOD (Wan et al., 2024), which uses 500 rounds with five epochs of local training per round. Kim et al.’s (Kim et al., 2024) method goes even further, using 1,000 rounds with a fixed 80 steps of local training per round.

In our setup, both traditional FL methods and ConDistFL were configured to use 120 rounds with 1,000 local training steps per round in the 3D experiments and 30 rounds with 500 local training steps per round in the 2D experiments. Despite the lower aggregation rounds, ConDistFL and traditional FL methods produced competitive global models, as demonstrated by the in-federation test results in Table 4. These findings challenge the assumption that higher aggregation frequencies are necessary for partially labeled FL scenarios. Instead, our results suggest that a well-tuned training configuration is more important for performance. Reducing the number of aggregation rounds not only avoids performance degradation but also significantly reduces communication traffic, improving the overall efficiency of the FL system.

## 6.5 Limitation

Despite ConDistFL’s strong performance in tumor segmentation on datasets with detailed lesion annotations, such as KiTS19 and MSD, the out-of-federation AMOS22 dataset lacks specific annotations for lesions, limiting the ability to evaluate the model’s performance on tumor segmentation in that context. This absence of lesion ground truth in some datasets, rather than a shortcoming of the model itself, prevents us from fully assessing its tumor segmentation capabilities across all testing scenarios. Future work could integrate multi-modal data or diagnostic information to further enhance lesion detection in datasets that lack lesion annotations.

## 6.6 Conclusion

In this paper, we introduced ConDistFL, a novel federated learning framework that integrates conditional distillation to address the challenges of partial labeling in medical image segmentation. By combining marginal loss with the ConDist loss, ConDistFL effectively mitigates catastrophic forgetting and model divergence,

significantly enhancing segmentation performance across distributed datasets.

Through extensive experiments on 3D abdominal CT and 2D chest X-ray datasets, ConDistFL consistently outperformed both state-of-the-art FL methods and standalone models, achieving higher Dice scores in both in-federation and out-of-federation test scenarios. A notable strength of ConDistFL is its ability to maintain computational and communication efficiency, ensuring scalability for real-world applications, even in challenging conditions with unseen contrast phases.

While the framework incurs a modest increase in training time, the substantial performance gains and generalizability more than compensate for this overhead. However, we recognize limitations in lesion segmentation due to the absence of detailed pathological annotations. Future work could address this by incorporating multi-modal data and exploring advanced strategies for lesion-specific learning, further enhancing the clinical applicability of ConDistFL.

Overall, ConDistFL offers a robust, scalable, and generalizable solution for federated learning in medical image segmentation, providing improved accuracy and flexibility across diverse medical imaging environments.

## Declaration of Generative AI and AI-assisted Technologies in the Writing Process

The authors used ChatGPT to assist with language refinement during the preparation of this manuscript. All content generated by the tool was reviewed and edited by the authors, who take full responsibility for the final content of the published article.

## Acknowledgement

This work was supported by grants from the National Science and Technology Council, Taiwan (NSTC 112-2634-F-002-003- and NSTC 113-2123-M-002-017-), and the Ministry of Health and Welfare (MOHW113-TDU-B221-134003). We thank the National Center for High-performance Computing (NCHC) for providing

computational and storage resources. The kidney, liver, pancreas, and spleen icons in Figure 1 were created using resources from Flaticon.com.

## References

- Ansel, J., Yang, E., He, H., Gimelshein, N., Jain, A., Voznesensky, M., Bao, B., Bell, P., Berard, D., Burovski, E., Chauhan, G., Chourdia, A., Constable, W., Desmaison, A., DeVito, Z., Ellison, E., Feng, W., Gong, J., Gschwind, M., Hirsh, B., Huang, S., Kalambarakar, K., Kirsch, L., Lazos, M., Lezcano, M., Liang, Y., Liang, J., Lu, Y., Luk, C., Maher, B., Pan, Y., Puhersch, C., Reso, M., Saroufim, M., Siraichi, M.Y., Suk, H., Suo, M., Tillet, P., Wang, E., Wang, X., Wen, W., Zhang, S., Zhao, X., Zhou, K., Zou, R., Mathews, A., Chanan, G., Wu, P., Chintala, S., 2024. Pytorch 2: Faster machine learning through dynamic python bytecode transformation and graph compilation, in: 29th ACM International Conference on Architectural Support for Programming Languages and Operating Systems, Volume 2 (ASPLOS '24), ACM. URL: <https://pytorch.org/assets/pytorch2-2.pdf>, doi:10.1145/3620665.3640366.
- Antonelli, M., Reinke, A., Bakas, S., Farahani, K., AnnetteKopp-Schneider, Landman, B.A., Litjens, G., Menze, B., Ronneberger, O., Summers, R.M., van Ginneken, B., Bilello, M., Bilic, P., Christ, P.F., Do, R.K.G., Gollub, M.J., Heckers, S.H., Huisman, H., Jarnagin, W.R., McHugo, M.K., Napel, S., Goli Pernicka, J.S., Rhode, K., Tobon-Gomez, C., Vorontsov, E., Huisman, H., Meakin, J.A., Ourselin, S., Wiesenfarth, M., Arbelaez, P., Bae, B., Chen, S., Daza, L., Feng, J., He, B., Isensee, F., Ji, Y., Jia, F., Kim, N., Kim, I., Merhof, D., Pai, A., Park, B., Perslev, M., Rezaifar, R., Rippel, O., Sarasua, I., Shen, W., Son, J., Wachinger, C., Wang, L., Wang, Y., Xia, Y., Xu, D., Xu, Z., Zheng, Y., Simpson, A.L., Maier-Hein, L., Jorge Cardoso, M., 2021. The medical segmentation decathlon. arXiv [eess.IV] .
- Candemir, S., Jaeger, S., Palaniappan, K., Musco, J.P., Singh, R.K., Zhiyun Xue, Karargyris, A., Antani, S., Thoma, G., McDonald, C.J., 2014. Lung segmentation in chest radiographs using anatomical atlases with nonrigid registration. *IEEE Trans. Med. Imaging* 33, 577–590.
- Chen, L.C., Papandreou, G., Schroff, F., Adam, H., 2017. Rethinking atrous convolution for semantic image segmentation. arXiv [cs.CV] .
- Czeizler, E., Wiessler, W., Koester, T., Hakala, M., Basiri, S., Jordan, P., Kuusela, E., 2020. Using federated data sources and varian learning portal framework to train a neural network model for automatic organ segmentation. *Phys. Med.* 72, 39–45.
- Dayan, I., Roth, H.R., Zhong, A., Harouni, A., Gentili, A., Abidin, A.Z., Liu, A., Costa, A.B., Wood, B.J., Tsai, C.S., Wang, C.H., Hsu, C.N., Lee, C.K., Ruan, P., Xu, D., Wu, D., Huang, E., Kitamura, F.C., Lacey, G., de Antônio Corradi, G.C., Nino, G., Shin, H.H., Obinata, H., Ren, H., Crane, J.C., Tetreault, J., Guan, J., Garrett, J.W., Kaggie, J.D., Park, J.G., Dreyer, K., Juluru, K., Kersten, K., Rockenbach, M.A.B.C., Linguraru, M.G., Haider, M.A., AbdelMaseeh, M., Rieke, N., Damasceno, P.F., E Silva, P.M.C., Wang, P., Xu, S., Kawano, S., Sriswasdi, S., Park, S.Y., Grist, T.M., Buch, V., Jantarabenjakul, W., Wang, W., Tak, W.Y., Li, X., Lin, X., Kwon, Y.J., Quraini, A., Feng, A., Priest, A.N., Turkbey, B., Glicksberg, B., Bizzo, B., Kim, B.S., Tor-Díez, C., Lee, C.C., Hsu, C.J., Lin, C., Lai, C.L., Hess, C.P., Compas, C., Bhatia, D., Oermann, E.K., Leibovitz, E., Sasaki, H., Mori, H., Yang, I., Sohn, J.H., Murthy, K.N.K., Fu, L.C., de Mendonça, M.R.F., Fralick, M., Kang, M.K., Adil, M., Gangai, N., Vateekul, P., Elnajjar, P., Hickman, S., Majumdar, S., McLeod, S.L., Reed, S., Gräf, S., Harmon, S., Kodama, T., Puthanakit, T., Mazzulli, T., de Lavor, V.L., Rakvongthai, Y., Lee, Y.R., Wen, Y., Gilbert, F.J., Flores, M.G., Li, Q., 2021. Federated learning for predicting clinical outcomes in patients with COVID-19. *Nat. Med.* 27, 1735–1743.
- Dou, Q., So, T.Y., Jiang, M., Liu, Q., Vardhanabhuti, V., Kaissis, G., Li, Z., Si, W., Lee, H.H.C., Yu, K., Feng, Z., Dong, L., Burian, E., Jungmann, F., Braren, R., Makowski, M., Kainz, B., Rueckert, D., Glocker, B.,

- Yu, S.C.H., Heng, P.A., 2021. Federated deep learning for detecting COVID-19 lung abnormalities in CT: a privacy-preserving multinational validation study. *NPJ Digit. Med.* 4, 60.
- Fang, X., Yan, P., 2020. Multi-organ segmentation over partially labeled datasets with multi-scale feature abstraction. *IEEE Transactions on Medical Imaging* 39, 3619–3629.
- Hatamizadeh, A., Nath, V., Tang, Y., Yang, D., Roth, H.R., Xu, D., 2021. Swin unetr: Swin transformers for semantic segmentation of brain tumors in mri images, in: *International MICCAI brainlesion workshop*, Springer. pp. 272–284.
- Hatamizadeh, A., Tang, Y., Nath, V., Yang, D., Myronenko, A., Landman, B., Roth, H.R., Xu, D., 2022. Unetr: Transformers for 3d medical image segmentation, in: *Proceedings of the IEEE/CVF winter conference on applications of computer vision*, pp. 574–584.
- Heller, N., Isensee, F., Maier-Hein, K.H., Hou, X., Xie, C., Li, F., Nan, Y., Mu, G., Lin, Z., Han, M., Yao, G., Gao, Y., Zhang, Y., Wang, Y., Hou, F., Yang, J., Xiong, G., Tian, J., Zhong, C., Ma, J., Rickman, J., Dean, J., Stai, B., Tejpaul, R., Oestreich, M., Blake, P., Kaluzniak, H., Raza, S., Rosenberg, J., Moore, K., Walczak, E., Rengel, Z., Edgerton, Z., Vasdev, R., Peterson, M., McSweeney, S., Peterson, S., Kalapara, A., Sathianathan, N., Papanikolopoulos, N., Weight, C., 2021. The state of the art in kidney and kidney tumor segmentation in contrast-enhanced ct imaging: Results of the kits19 challenge. *Medical Image Analysis* 67, 101821. doi:<https://doi.org/10.1016/j.media.2020.101821>.
- Isensee, F., Jaeger, P.F., Kohl, S.A., Petersen, J., Maier-Hein, K.H., 2021. nnu-net: a self-configuring method for deep learning-based biomedical image segmentation. *Nature methods* 18, 203–211.
- Isensee, F., Wald, T., Ulrich, C., Baumgartner, M., Roy, S., Maier-Hein, K., Jaeger, P.F., 2024. NnU-net revisited: A call for rigorous validation in 3D medical image segmentation. *arXiv [cs.CV]* .
- Jaeger, S., Candemir, S., Antani, S., Wang, Y.X.J., Lu, P.X., Thoma, G., 2014a. Two public chest X-ray datasets for computer-aided screening of pulmonary diseases. *Quant. Imaging Med. Surg.* 4, 475–477.
- Jaeger, S., Karargyris, A., Candemir, S., Folio, L., Siegelman, J., Callaghan, F., Zhiyun Xue, Palaniappan, K., Singh, R.K., Antani, S., Thoma, G., Yi-Xiang Wang, Pu-Xuan Lu, McDonald, C.J., 2014b. Automatic tuberculosis screening using chest radiographs. *IEEE Trans. Med. Imaging* 33, 233–245.
- Ji, Y., Bai, H., Yang, J., Ge, C., Zhu, Y., Zhang, R., Li, Z., Zhang, L., Ma, W., Wan, X., et al., 2022. Amos: A large-scale abdominal multi-organ benchmark for versatile medical image segmentation. *arXiv preprint arXiv:2206.08023* .
- Ji, Z., Guo, D., Wang, P., Yan, K., Lu, L., Xu, M., Zhou, J., Wang, Q., Ge, J., Gao, M., Ye, X., Jin, D., 2023. Continual segment: Towards a single, unified and accessible continual segmentation model of 143 whole-body organs in CT scans. *arXiv [cs.CV]* .
- Jorge Cardoso, M., Li, W., Brown, R., Ma, N., Kerfoot, E., Wang, Y., Murrey, B., Myronenko, A., Zhao, C., Yang, D., Nath, V., He, Y., Xu, Z., Hatamizadeh, A., Myronenko, A., Zhu, W., Liu, Y., Zheng, M., Tang, Y., Yang, I., Zephyr, M., Hashemian, B., Alle, S., Darestani, M.Z., Budd, C., Modat, M., Vercauteren, T., Wang, G., Li, Y., Hu, Y., Fu, Y., Gorman, B., Johnson, H., Genereaux, B., Erdal, B.S., Gupta, V., Diaz-Pinto, A., Dourson, A., Maier-Hein, L., Jaeger, P.F., Baumgartner, M., Kalpathy-Cramer, J., Flores, M., Kirby, J., Cooper, L.A.D., Roth, H.R., Xu, D., Bericat, D., Floca, R., Kevin Zhou, S., Shuaib, H., Farahani, K., Maier-Hein, K.H., Aylward, S., Dogra, P., Ourselin, S., Feng, A., 2022. MONAI: An open-source framework for deep learning in healthcare. *arXiv [cs.LG]* .



- Kim, S., Park, H., Kang, M., Jin, K.H., Adeli, E., Pohl, K.M., Park, S.H., 2024. Federated learning with knowledge distillation for multi-organ segmentation with partially labeled datasets. *Med. Image Anal.* 95, 103156.
- Landman, B., Xu, Z., Igelsias, J., Styner, M., Langerak, T., Klein, A., 2015. Miccai multi-atlas labeling beyond the cranial vault—workshop and challenge, in: *Proc. MICCAI Multi-Atlas Labeling Beyond Cranial Vault—Workshop Challenge*, p. 12.
- Li, T., Sahu, A.K., Zaheer, M., Sanjabi, M., Talwalkar, A., Smith, V., 2020. Federated optimization in heterogeneous networks. *Proceedings of Machine learning and systems 2*, 429–450.
- Li, W., Milletari, F., Xu, D., Rieke, N., Hancox, J., Zhu, W., Baust, M., Cheng, Y., Ourselin, S., Cardoso, M.J., Feng, A., 2019. Privacy-preserving federated brain tumour segmentation, in: *Machine Learning in Medical Imaging*. Springer International Publishing, Cham. Lecture notes in computer science, pp. 133–141.
- Liu, H., Xu, Z., Gao, R., Li, H., Wang, J., Chabin, G., Oguz, I., Grbic, S., 2024. Cosst: Multi-organ segmentation with partially labeled datasets using comprehensive supervisions and self-training. *IEEE Transactions on Medical Imaging* .
- Liu, J., Zhang, Y., Chen, J.N., Xiao, J., Lu, Y., Landman, B., Yuan, Y., Yuille, A., Tang, Y., Zhou, Z., 2023. Clip-driven universal model for organ segmentation and tumor detection, in: *Proceedings of the IEEE/CVF International Conference on Computer Vision*, pp. 21152–21164.
- Liu, P., Wang, X., Fan, M., Pan, H., Yin, M., Zhu, X., Du, D., Zhao, X., Xiao, L., Ding, L., Wu, X., Zhou, S.K., 2022. Learning incrementally to segment multiple organs in a CT image, in: *Medical Image Computing and Computer Assisted Intervention – MICCAI 2022*, Springer Nature Switzerland. pp. 714–724.
- McMahan, B., Moore, E., Ramage, D., Hampson, S., y Arcas, B.A., 2017. Communication-efficient learning of deep networks from decentralized data, in: *Artificial intelligence and statistics*, PMLR. pp. 1273–1282.
- Milletari, F., Navab, N., Ahmadi, S., 2016. V-net: Fully convolutional neural networks for volumetric medical image segmentation, in: *2016 Fourth International Conference on 3D Vision (3DV)*, IEEE Computer Society, Los Alamitos, CA, USA. pp. 565–571. URL: <https://doi.ieeecomputersociety.org/10.1109/3DV.2016.79>, doi:10.1109/3DV.2016.79.
- Rajaraman, S., Folio, L.R., Dimperio, J., Alderson, P.O., Antani, S.K., 2021. Improved semantic segmentation of tuberculosis-consistent findings in chest X-rays using augmented training of modality-specific U-net models with weak localizations. *Diagnostics (Basel)* 11, 616.
- Reddi, S., Charles, Z., Zaheer, M., Garrett, Z., Rush, K., Konečný, J., Kumar, S., McMahan, H.B., 2020. Adaptive federated optimization. *arXiv preprint arXiv:2003.00295* .
- Rieke, N., Hancox, J., Li, W., Milletari, F., Roth, H.R., Albarqouni, S., Bakas, S., Galtier, M.N., Landman, B.A., Maier-Hein, K., et al., 2020. The future of digital health with federated learning. *NPJ digital medicine* 3, 1–7.
- Ronneberger, O., Fischer, P., Brox, T., 2015. U-net: Convolutional networks for biomedical image segmentation, in: *Medical image computing and computer-assisted intervention—MICCAI 2015: 18th international conference, Munich, Germany, October 5-9, 2015, proceedings, part III 18*, Springer. pp. 234–241.

- Roth, H.R., Cheng, Y., Wen, Y., Yang, I., Xu, Z., Hsieh, Y.T., Kersten, K., Harouni, A., Zhao, C., Lu, K., Zhang, Z., Li, W., Myronenko, A., Yang, D., Yang, S., Rieke, N., Quraini, A., Chen, C., Xu, D., Ma, N., Dogra, P., Flores, M., Feng, A., 2023. Nvidia flare: Federated learning from simulation to real-world. *IEEE Data Eng. Bull.*, Vol. 46, No. 1 doi:<https://doi.org/10.48550/arXiv.2210.13291>.
- Roy, S., Koehler, G., Ulrich, C., Baumgartner, M., Petersen, J., Isensee, F., Jaeger, P.F., Maier-Hein, K.H., 2023a. Mednext: transformer-driven scaling of convnets for medical image segmentation, in: *International Conference on Medical Image Computing and Computer-Assisted Intervention*, Springer. pp. 405–415.
- Roy, S., Koehler, G., Ulrich, C., Baumgartner, M., Petersen, J., Isensee, F., Jäger, P.F., Maier-Hein, K.H., 2023b. Mednext: Transformer-driven scaling of convnets for medical image segmentation, in: Greenspan, H., Madabhushi, A., Mousavi, P., Salcudean, S., Duncan, J., Syeda-Mahmood, T., Taylor, R. (Eds.), *Medical Image Computing and Computer Assisted Intervention – MICCAI 2023*, Springer Nature Switzerland, Cham. pp. 405–415.
- Sheller, M.J., Reina, G.A., Edwards, B., Martin, J., Bakas, S., 2019. Multi-institutional deep learning modeling without sharing patient data: A feasibility study on brain tumor segmentation. *Brainlesion 11383*, 92–104.
- Shen, C., Wang, P., Yang, D., Xu, D., Oda, M., Chen, P.T., Liu, K.L., Liao, W.C., Fuh, C.S., Mori, K., et al., 2022. Joint multi organ and tumor segmentation from partial labels using federated learning, in: *International Workshop on Distributed, Collaborative, and Federated Learning*, Springer. pp. 58–67.
- Shi, G., Xiao, L., Chen, Y., Zhou, S.K., 2021. Marginal loss and exclusion loss for partially supervised multi-organ segmentation. *Medical Image Analysis* 70, 101979. URL: <https://www.sciencedirect.com/science/article/pii/S1361841521000256>, doi:<https://doi.org/10.1016/j.media.2021.101979>.
- Shiraishi, J., Katsuragawa, S., Ikezoe, J., Matsumoto, T., Kobayashi, T., Komatsu, K., Matsui, M., Fujita, H., Kodera, Y., Doi, K., 2000. Development of a digital image database for chest radiographs with and without a lung nodule: receiver operating characteristic analysis of radiologists’ detection of pulmonary nodules: Receiver operating characteristic analysis of radiologists’ detection of pulmonary nodules. *AJR Am. J. Roentgenol.* 174, 71–74.
- Correia de Verdier, M., Saluja, R., Gagnon, L., LaBella, D., Baid, U., Tahon, N.H., Foltyn-Dumitru, M., Zhang, J., Alaff, M., Baig, S., Chang, K., D’Anna, G., Deptula, L., Gupta, D., Haider, M.A., Hussain, A., Iv, M., Kontzialis, M., Manning, P., Rudie, J., 2024. The 2024 brain tumor segmentation (brats) challenge: Glioma segmentation on post-treatment mri doi:10.48550/arXiv.2405.18368.
- Wan, Q., Yan, Z., Yu, L., 2024. Fediod: Federated multi-organ segmentation from partial labels by exploring inter-organ dependency. *IEEE Journal of Biomedical and Health Informatics* .
- Wang, P., Shen, C., Roth, H.R., Yang, D., Xu, D., Oda, M., Misawa, K., Chen, P.T., Liu, K.L., Liao, W.C., Wang, W., Mori, K., 2020. Automated pancreas segmentation using multi-institutional collaborative deep learning, in: *Domain Adaptation and Representation Transfer, and Distributed and Collaborative Learning*, Springer International Publishing. pp. 192–200.
- Wang, P., Shen, C., Wang, W., Oda, M., Fuh, C.S., Mori, K., Roth, H.R., 2023. Condistfl: Conditional distillation for federated learning from partially annotated data, in: *Medical Image Computing and Computer Assisted Intervention – MICCAI 2023 Workshops*, Springer Nature Switzerland, Cham. pp. 311–321.
- Wasserthal, J., Breit, H.C., Meyer, M.T., Pradella, M., Hinck, D., Sauter, A.W., Heye, T., Boll, D.T., Cyriac, J., Yang, S., Bach, M., Segeroth, M., 2023. TotalSegmentator: Robust segmentation of 104 anatomic structures in CT images. *Radiol. Artif. Intell.* 5, e230024.

- Woo, S., Debnath, S., Hu, R., Chen, X., Liu, Z., Kweon, I.S., Xie, S., 2023. Convnext v2: Co-designing and scaling convnets with masked autoencoders. arXiv preprint arXiv:2301.00808 .
- Xia, Y., Yang, D., Li, W., Myronenko, A., Xu, D., Obinata, H., Mori, H., An, P., Harmon, S., Turkbey, E., Turkbey, B., Wood, B., Patella, F., Stellato, E., Carrafiello, G., Ierardi, A., Yuille, A., Roth, H., 2021. Auto-FedAvg: Learnable federated averaging for multi-institutional medical image segmentation. arXiv [eess.IV] .
- Xie, Y., Zhang, J., Xia, Y., Shen, C., 2023. Learning from partially labeled data for multi-organ and tumor segmentation. IEEE Transactions on Pattern Analysis and Machine Intelligence .
- Xu, X., Deng, H.H., Gateno, J., Yan, P., 2023. Federated multi-organ segmentation with inconsistent labels. IEEE transactions on medical imaging 42, 2948–2960.
- Yang, Q., Liu, Y., Chen, T., Tong, Y., 2019. Federated machine learning: Concept and applications. ACM Transactions on Intelligent Systems and Technology (TIST) 10, 1–19.
- Yu, Q., Yang, D., Roth, H., Bai, Y., Zhang, Y., Yuille, A.L., Xu, D., 2020. C2fnas: Coarse-to-fine neural architecture search for 3d medical image segmentation, in: Proceedings of the IEEE/CVF Conference on Computer Vision and Pattern Recognition, pp. 4126–4135.
- Zawacki, A., Wn, C., Shih, G., Elliott, J., Fomitchev, M., Hussain, M., ParasLakhani, Culliton, P., Bao, S., 2019. Siim-acr pneumothorax segmentation. Kaggle. .
- Zhang, J., Xie, Y., Xia, Y., Shen, C., 2021. Dodnet: Learning to segment multi-organ and tumors from multiple partially labeled datasets, in: Proceedings of the IEEE conference on computer vision and pattern recognition.
- Zhou, Z., Siddiquee, M.M.R., Tajbakhsh, N., Liang, J., 2018. UNet++: A nested U-net architecture for medical image segmentation. arXiv [cs.CV] .